Nanoscale Advances

ROYAL SOCIETY OF CHEMISTRY

PAPER

View Article Online
View Journal | View Issue

Cite this: *Nanoscale Adv.*, 2023, **5**, 5131

Raman spectroscopy of a few layers of bismuth telluride nanoplatelets†

Victor Carozo, *[a] Bruno R. Carvalho, [b] Syed Hamza Safeer, [c] Leandro Seixas, [d] Pedro Venezuela[e] and Mauricio Terrones [f]

We can shape the electronic and phonon properties of Bi_2Te_3 crystals *via* the variation of the number of layers. Here, we report a Raman study with the aid of first-principles calculations on few-layered Bi_2Te_3 systems ranging from 5 to 24 nm layer thickness using 1.92, 2.41 and 2.54 eV excitation energies. We examine how the frequency position, intensity and lineshape of the main Raman modes (A^1_{1g}, E^2_g, and A^2_{1g}) behave by the variation of the layer thickness and excitation energy. We observed a frequency dispersion on the number of layers of the main modes, indicating changes in the inter- and intra-layers interaction. A resonant Raman condition is reached for all modes for samples with 11 and 18 nm thickness because of van Hove singularities at the electronic density of states. Also, the Breit–Wigner–Fano line shape of the A^2_{1g} mode shows an increase of electron–phonon coupling for thick layers. These results suggest a relevant influence of numbers of layers on the Raman scattering mechanics in Bi_2Te_3 systems.

Received 1st August 2023
Accepted 18th August 2023

DOI: 10.1039/d3na00585b

rsc.li/nanoscale-advances

Introduction

Three-dimensional topological insulator (TI) bismuth telluride (Bi_2Te_3) exhibits an insulating gap in its bulk form. However, it becomes gapless at the edges where a Dirac cone is formed.[1] Moreover, it presents opposite spin states at the edges that propagate in opposite directions.[2–4] Intriguing new physics phenomena emerge from this new quantum matter state, such as Majorana fermions,[5] quantum spin Hall,[6] and fractional charged and quantized current.[1,7] Besides, the metallic character of the edge states unlocks possible spintronics and quantum computation applications.[4] Experimentally, it is common to find a conductive bulk instead of edges dominating the electronic transport because of defects.[8,9] Added to defects, the number of layers also plays an essential role in reaching the non-trivial topological states.[10] It has been reported that few-layered Bi_2Te_3 presents a parabolic electronic band crossing at the Fermi level and depicts a trivial topological state.[10–12] When the Bi_2Te_3 crystal has five or more layers, one observes a M-like shape valence band and Dirac surface states in the conduction band at the Γ point, which represents the non-trivial topological state.[13–15] Furthermore, the non-trivial topological insulating phase can be induced by the electron–phonon coupling in TI materials with narrow bandgaps,[16,17] becoming fundamental to their investigation.

In this context, finding means to probe the changes in the properties of a few layers in this system is fundamental. Raman spectroscopy is a simple, fast, and non-invasive technique widely used to probe phonons and their interactions with electrons in layered materials.[18] Conventionally, the Raman scattering involves phonons with momentum $\mathbf{q} = 0$ at the center of the Brillouin zone (BZ), *i.e.*, the Γ point. This process is known as the first-order process since only one phonon is involved in the scattering. However, when excitation laser energy matches the energy bandgap of van Hove singularities (vHs), the scattering event's probability increases, reaching a resonance scattering condition and, observed by one enchantment of Raman counts.[19] Besides, one can relax the selection rules[20] ($\mathbf{q} = 0$) by different means such as doping, isotope modulation, disorder, and thickness variation.[3,21–25] As a result, we could note a shift in the Raman frequencies. In particular, the asymmetric Breit–Wigner–Fano (BWF) line shape can probe the phonon coupling to a continuum of collective excitations of the electrons. It can be used to estimate the electron–phonon coupling strength.[20,26,27] Despite the versatility of Raman spectroscopy, a study involving thickness variation, resonance Raman scattering, and estimation of electron–

[a]*Department of Physics, Pontifical Catholic University of Rio de Janeiro, Rio de Janeiro, RJ 22451900, Brazil. E-mail: vcarozo@puc-rio.br*

[b]*Departamento de Física, Universidade Federal do Rio Grande do Norte, Natal, Rio Grande do Norte, RN 59078-970, Brazil*

[c]*Department of Physics, Materials Science Lab, Quaid-i-Azam University, Islamabad, 45320, Pakistan*

[d]*School of Engineering, Mackenzie Presbyterian University, Rua da Consolação, 930, São Paulo, SP 01302-907, Brazil*

[e]*Institute of Physics, Fluminence Federal University, Niteroi, RJ, 24210-346, Brazil*

[f]*Department of Physics and Department of Materials Science and Engineering, The Pennsylvania State University, University Park, PA 16802, USA*

† Electronic supplementary information (ESI) available. See DOI: https://doi.org/10.1039/d3na00585b

phonon coupling in a continuum of Bi_2Te_3 multiple layers has not been determined.

In the present study, we synthesized multiple layered Bi_2Te_3 and probed the phonon properties and their interactions with electrons *via* Raman spectroscopy with the aid of density functional theory (DFT) calculations. We observed three main Raman modes: A^1_{1g}, E^2_g and A^2_{1g} for layers with thickness between 5 to 24 nm, and their frequency variation with the crystal's number of layers indicates phonon confinement. We noticed that for Bi_2Se_3 crystal with thickness of 11–18 nm, the Raman spectrum shows a resonant Raman condition when excited with a laser energy of 1.92 eV for all Raman modes. The BWF line shapes show that the electron–phonon coupling becomes prominent as the number of layer increases due to the interference effect between the phonon spectra and the electron–hole pair excitation spectra at a vHs in the density of states. Our findings indicate the impact of the number of layers on the phonon and electronic properties of Bi_2Te_3.

Materials and methods

The layered Bi_2Te_3 were grown at low-atmospheric pressure by vapor phase deposition (LPVPD) onto silicon wafers of 300 nm SiO_2 layer thickness, as reported elsewhere.[28–31] An alumina boat containing 10 mg of Bi_2Te_3 (Alfa Aesar, 99.5%) was located at the center of the furnace, and a SiO_2/Si substrate was placed 18 cm from the boat upstream. The furnace was heated up to 480 °C for 30 min, and the temperature of the substrate was held at around 200 °C. Then, the system was kept at a dwell time of 30 min. A 10 sccm of Argon flux was used during the synthesis process, and the pressure was set to 100 mTorr (see ESI Fig. S1† for optical images of the as-grown crystals). The number of layers was characterized by atomic force microscopy (AFM) using NanoMagnetics Instruments at ambient conditions operated in tapping mode. The step heights were measured through line scans to determine the thickness.

The Raman measurements were conducted in a Renishaw inVia microscope with a Coherent Innova 70C Argon–Krypton laser with excitation energies of 2.54 eV (488 nm), 2.41 eV (514 nm), and 1.92 eV (647 nm). All spectra were collected in the back-scattering geometry using an 1800 lines per mm grating and an Olympus 100 × (0.95 NA) objective lens. The laser power density was measured with Thorlabs optical power meter and kept below 50 μW to avoid sample damage.

The density-functional calculations (DFT) were performed with the Quantum ESPRESSO code (QE)[32] using the projector augmented plane wave (PAW) method[33] and the Perdew–Zunger[34] and Perdew–Burke–Ernzerhof[35] exchange–correlation functionals within the local density (LDA) and generalized gradient approximations (GGA), respectively.

Results and discussion

A layered Bi_2Te_3 exhibits a rhombohedral lattice structure belonging to the D^5_{3d} point group ($R\bar{3}m$ space group).[36,37] Its atomic arrangement can be seen as the stacking of five monoatomic layers covalently bonded to one another with a Bi-Te-Bi-Te-Bi sequence along the *c*-axis, as shown in Fig. 1a. This five-monoatomic arrangement is referred to as quintuple layers (QLs) and has 0.96 nm of thickness. Each QL is bonded together by van der Waals interactions, and inside a QL, the Bi–Te bond is the strongest, while the Te–Te bond is the weakest. Therefore, the coupling between two atomic layers inside a QL is more robust than those outside of a QL.[8,38–40] The as-grow Bi_2Te_3 QLs are isolated crystals covering the substrate with variate geometries, such as triangular, hexagonal, and truncated triangles (see ESI Fig. S1†), known as nanoplatelets. Fig. 1b shows an AFM image of a hexagonal-shaped nanoplatelet with a thickness of about 5 nm, which is equivalent to 5 QLs measured by the line profile (see bottom panel). Additional AFM images are shown in ESI Fig. S1.†

The primitive cell of a QL Bi_2Te_3 has 5 atoms. Thus group theory predicts three acoustic and 12 optical branches at the center of BZ, $\mathbf{\Gamma}$ ($\mathbf{q} = 0$), and its irreducible representation is $\mathbf{\Gamma} = 2E_g \oplus 2A_{1g} \oplus 2E_u \oplus 2A_{1u}$, where E_g and E_u modes are twofold degenerates. Only the $2E_g \oplus 2A_{1g}$ are Raman active.[38,39] To investigate the influence of the number of layers in the vibrational properties of Bi_2Te_3, we collected the Raman spectrum for samples with thicknesses from 5 up to 24 nm with excitation energy of 1.92 eV. Fig. 1c shows the intensity map of the Raman spectra as a function of thickness, where the colors represent the intensity, yellow for the highest. One can notice three first-order Raman modes located at around 50 cm^{-1}, 100 cm^{-1} and 135 cm^{-1} assigned, respectively, as A^1_{1g}, E^2_g, and A^2_{1g}. The A^1_{1g} and A^2_{1g} modes correspond to out-of-plane vibrations, while the E^2_g doubly degenerated mode corresponds to in-plane vibrations (see inset in Fig. 1c). In the A^1_{1g} mode symmetry, the atoms move in phase while the atoms pairs move in opposite phase for the E^2_{2g} and A^2_{1g} modes. We comment that due to the notch filter limit used in our experiment, it was not possible to investigate the Raman modes below 50 cm^{-1}, where the E^1_g mode (35 cm^{-1})[29] is located. We notice a deviation in these modes' frequency as the layer is reduced. In addition, one can observe an emerged Raman peak of the lower wavenumber shoulder of the E^2_g mode, as shown in Fig. 1d for a sample with 6 nm QL thickness. This Raman peak is located at around 95 cm^{-1} and only appears for layers lower than 9 nm. The break of double degenerescence of E^2_g modes could be associated with increased strain as the number of layers decreases. It is worth of note that all modes present a high intensity for samples of around 10 nm QL thickness. In Fig. 1d, one also observes an asymmetry in the line shape of the A^2_{1g} mode.

Fig. 2a–c show the Raman frequency position of the A^1_{1g}, E^2_g, and A^2_{1g} modes as a function of the number of layers for the three excitation energies 1.92 eV, 2.41 eV, and 2.54 eV. The frequency position of each mode was extracted from fitting the Raman spectra using the Lorentzian function (see ESI Figures S2–S4†). We can observe that the frequency position of the A^2_{1g} mode downshifts when increases the number of layers and exhibits a linear behavior for all excitation energies. This dispersion was fitted by straight lines, and the slopes of the number of layers dependence for the A^2_{1g} modes are −0.21, −0.16 and −0.06 cm^{-1}/L (nm) for, respectively, the 1.92, 2.41 and 2.54 eV laser excitation energies. Here, *L* (nm) corresponds

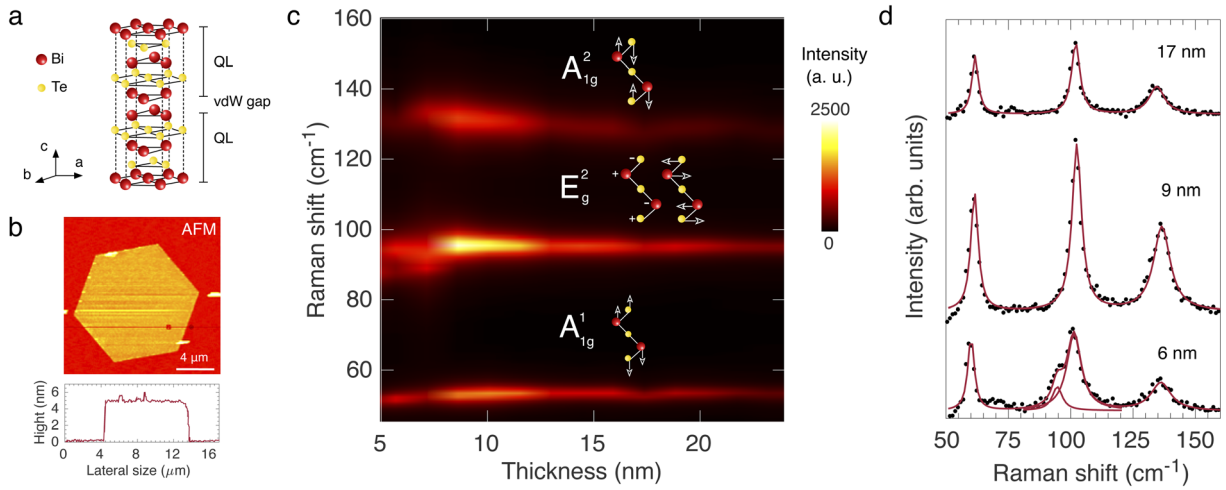

Fig. 1 (a) Crystalline structure of Bi_2Te_3, 1 QL = 0.96 nm. (b) (Top) AFM topography image of hexagonal nanoplatelet with 5 nm QL thickness. Bottom: Line cross-section showing the step height. (c) Intensity map of Raman spectra for a few QLs using excitation laser energy of 1.92 eV, the orange and yellow regions indicate the position of A^2_{1g}, E^2_g, and A^1_{1g} modes. (d) Raman spectra for 6, 9, and 17 nm of crystal thickness withdrawn from (a), the lines are the adjusted curves.

to the QL thickness. Note that the slope decreases as the excitation energy increases. Intriguingly, the frequency position of the A^1_{1g} and E^2_g modes upshift as the number of layers increases, and they become almost constant for thickness above 9 nm; here the lines in these modes are a guide to the eye. The open circles in Fig. 2a are the position of the second peak near E^2_g due to split. The A^1_{1g} mode is absent for 2.54 eV excitation laser energy.

Raman modes are expected to stiffen as an outcome of the confined phonon by the reduction of the number of layers. In this case, the interlayer van der Waals interactions increase the influential restoring forces acting on out-of-plane atoms, thus affecting the frequency of A^1_{1g} and A^2_{1g} modes. The shift of in-plane E^2_g mode may be attributable to long-range Coulomb interlayer interactions.[20,41] This finding suggests that the QL stacking also affects the intralayer bonding. To verify this, we performed phonon dispersion calculations based on density functional perturbation theory (DFPT)[42] implemented in Quantum Espresso. We examined the phonon dispersion branch of the A^1_{1g}, E^2_g, and A^2_{1g} modes along the Γ–Z direction using the LDA and GGA methods as shown in Fig. 2d. Note that the LDA phonon frequencies are overestimated, while the GGA is underestimated. We observe that the A^1_{1g} mode redshifts along the Γ–Z direction in agreement with the experimental result, while the A^2_{1g} mode exhibits an opposite behavior. The reason may be related to the restoring forces as the number of layers decreases. However, further theoretical aid would be required to fully understand this behavior. We also comment that the calculation uncertainty is less than 5 cm^{-1}. The E^2_g mode does not show dispersion because the calculation was taken only along the out-of-plane direction, thus not enabling us to observe variation for the in-plane mode.

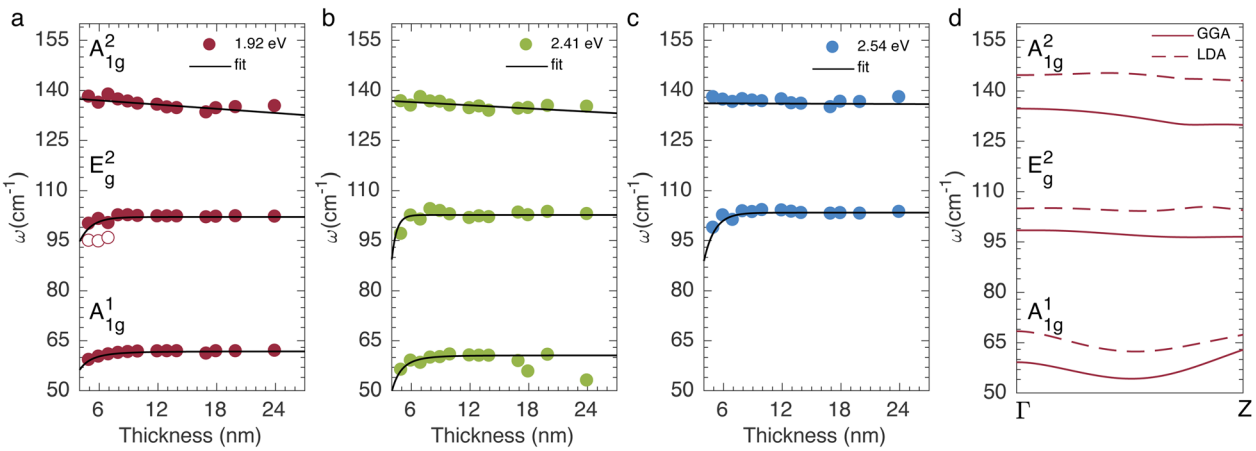

Fig. 2 (a–c) The frequency position of A^2_{1g}, E^2_g, and A^1_{1g} modes as a function of QL thickness for excitation laser energies of 1.92, 2.41 and 2.54 eV, respectively. The lines in A^1_{1g} and E^2_g modes are a guide to the eye. (d) DFPT calculation of phonons dispersion a long of Γ–Z direction employing the LDA and GGA approximations.

We now examine the intensity enhancement effects of A_{1g}^2, E_g^2, and A_{1g}^1 modes for, respectively, 1.92, 2.41, and 2.54 eV laser energies for crystals with 5 to 24 nm QL thickness. Fig. 3a–c show the normalized intensity of the first-order modes, A_{1g}^2, E_g^2, and A_{1g}^1 modes, as a function of the crystal's thickness. Two maxima at around 11–12 nm and 18 nm QL thickness are observed for the A_{1g}^2 mode at the 1.92 eV laser energy. These two maxima also appear at the 2.41 and 2.54 eV laser energies, respectively. However, their intensity enhancement is much lower than the 1.92 eV. These two maxima enhancements are also observed for the E_g^2 and A_{1g}^1 modes. Note that for the E_g^2 mode, there is a considerable enhancement for the 2.54 eV, but the A_{1g}^1 mode only exhibits strong enhancement for the 1.92 eV. Besides, notice that the A_{1g}^1 mode is absent for 2.54 eV due to the resonance conditions related to the fact that its electron–phonon matrix elements are small, see Fig. S4.†

These results are evidence of a resonant Raman scattering being achieved for the Bi_2Te_3, especially at 1.92 eV laser energy. The mechanism can be described by third-order time-dependent perturbation theory.[18,43] The main contribution for the intensity comes from resonance matching between excitation laser energy E_L and the separation of vHs in the density of states of the electronic dispersion, *i.e.*, $E_L = E_{vHs}$. Usually, the E_L dependence of the Raman intensity of the first-order mode is analyzed. However, in this work, the E_L is fixed, and the tuning of the electronic band structure is given by changing the E_{vHs} energy upon the variation in the number of layers. The Raman intensity resonance profile can be expressed by:[19]

$$I \propto \left| \sum_{a,b} \frac{\langle f|H_{er}|b\rangle\langle b|H_{ep}|a\rangle\langle a|H_{er}|i\rangle}{(E_L - E_a - i\gamma)(E_L - E_b - \hbar\omega_{\mathbf{q}} - i\gamma)} \right|^2, \quad (1)$$

where $\langle a|H_{er}|i\rangle$ and $\langle f|H_{er}|b\rangle$ are the electron–photon matrix elements for absorption and emission, respectively, and $\langle b|H_{ep}|a\rangle$ is the electron–phonon matrix elements involved in the intermediate scattering processes. The parameter γ is a damping constant associated with the finite lifetime of the intermediate states. The E_L, E_a, E_b are, respectively, the energy of the incident light and electronic states of the $|a\rangle$ and $|b\rangle$ states. The $\hbar\omega_{\mathbf{q}}$ represents the energy of a $\mathbf{q}$ phonon mode. A resonance phenomenon will occur whenever the $E_L = E_a$ or $E_L = E_b$ condition is satisfied.

Therefore, the enhancement observed for 11–12 nm QLs thickness using the excitation laser of 1.92 eV could be due to the matching of $E_L = E_{vHs}$. The electronic states are sensitive to the thickness in the Bi_2Te_3 system. To verify this, we calculated the density of states of multiple QLs thicknesses. The calculated density of states has van Hove singularities close to the top of the valence band and close to the bottom of the conduction band (see ESI Figures S5 and S6†). Fig. 3d shows the energy differences of the vHs as a function of the QL thickness. One can observe that the gap decreases by the increasing of the number of layers, and it presents a $E_{vHs} = 2$ eV for 10–12 nm QL thickness, indicating a quasi-matching to $E_L = 1.92$ eV. Therefore, explaining the observed enhancement of all modes.

By inspection of Fig. 1d, one observes that the A_{1g}^2 mode exhibits an asymmetric shape for varying QL thickness at 1.92 eV. To investigate this, we employed the BWF resonance line shape to fit the A_{1g}^2 mode and gain insights into the electron–phonon coupling strength. In short, the BWF resonance describes interactions between the one-phonon scattering process and one-electron excitation from filled to empty valence bands. This results in an asymmetrical line shape produced by the interference between the discrete and continuum scattering mechanisms.[20,26,27] Fig. 4a shows that the A_{1g}^2 mode has an asymmetric broadening in the line shape when the number of layers increases for the 1.92 eV. The A_{1g}^2 broadening line shape was fitted considering the following expression,

$$I_{A_{1g}^2}(\omega) = \frac{I_0(q + (\omega - \omega_0)/\Gamma)^2}{1 + [(\omega - \omega_0)/\Gamma]^2}, \quad (2)$$

where ω_0 is the renormalized A_{1g}^2 mode phonon frequency in the presence of the coupled scattering, q is the asymmetric parameter, and Γ is the width parameter and is related to the phonon lifetime. The parameter q determines the strength of the electronic scattering on the first-order phonon mode. It has

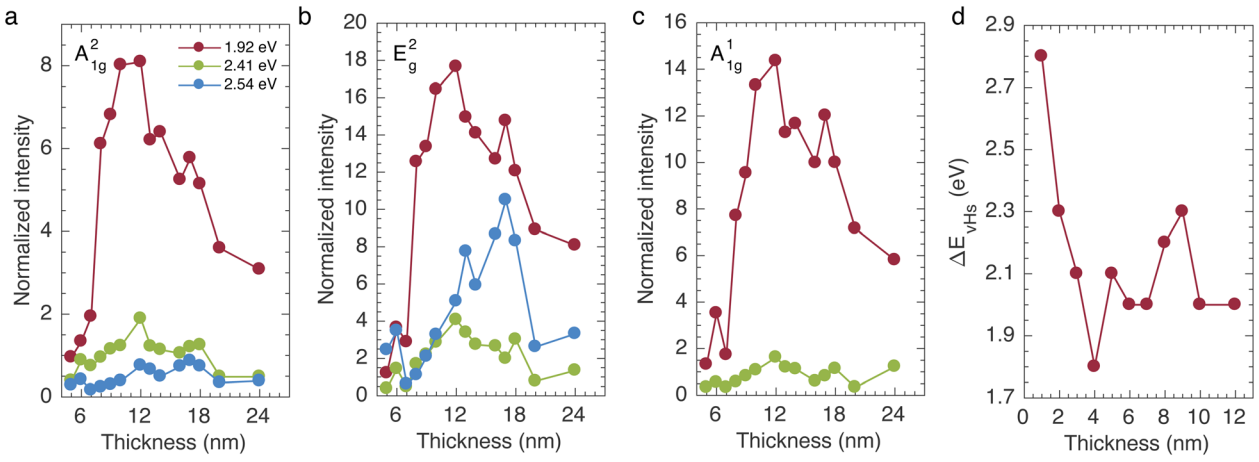

Fig. 3 (a–c) Intensity normalized by silicon peak of A_{1g}^2, E_g^2, and A_{1g}^1 modes as a function of QL thickness for excitation laser energies of 1.92 eV, 2.41 eV, and 2.54 eV, respectively. (d) The energy difference calculated between van Hove singularities (vHs) from 1 to 12 QLs.

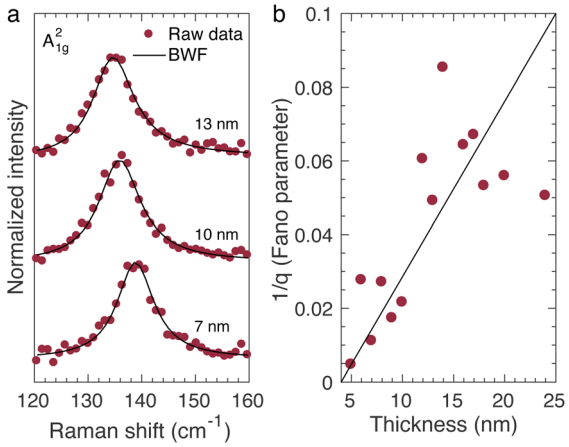

Fig. 4 (a) BWF line shape fitting and the experimental spectra of A^2_{1g} mode for 7, 10, 13 nm QL thickness. (b) Fano parameter $1/q$ dependence on the QL thickness, the line is a guide.

been shown that small values of q indicate a robust electron–phonon coupling.[20,44,45] Fig. 4b plots the $1/q$ parameter as a function of QL thickness for the A^2_{1g} modes. The $1/q$ is known as the Fano parameter, and it is obtained from fitting the phonon mode line shape (see black curves in Fig. 4a). The practical advantage of analyzing the $1/q$ parameter is due to the fact that in the $1/q \rightarrow 0$ limit, the BWF line shape becomes a Lorentzian function. From Fig. 4, we notice that the coupling parameter $1/q$ increases with the number of layers. Therefore, the asymmetric broadening of the A^2_{1g} mode may be associated with a Fano interference between the out-of-plane phonon mode and the electron–hole pair excitation spectra at a van Hove singularity in the density of states. These results indicate an enhancement of electron–phonon coupling when it increases the thickness from 5 to 24 QLs. Furthermore, the increase of electron–phonon coupling contributes positively to the resonance Raman scattering, a term present in the numerator of eqn (1).

Summary

To summarize, we have investigated a quasi-continuum range of a few quintuple layers of Bi_2Te_3 synthesized by LPVPD method using AFM and Raman spectroscopy with the aid of DFT calculations. Atomic force microscopy images were used to identify the crystal's thickness. The analyses of the Raman spectra revealed how the main modes (A^1_{1g}, E^2_g, and A^2_{1g}) in Bi_2Te_3 system behave by the variation of the number of layers and excitation energies. The frequency position of all main modes varies depending on the number of layers. The E^2_g and A^1_{1g} mode upshift upon the increasing of the number of layers. On the hand, the A^2_{1g} mode frequency downshift by the increasing of the number of layers, and with dispersive rates of -0.21, -0.16 and -0.06 cm^{-1}/L (nm) for 1.92, 2.41 and 2.54 eV excitation energies, respectively. The frequency variation of all main modes can be useful to identify the number of Bi_2Te_3 QL thickness, especially for QL thickness below 9 nm. In addition, we observed a degeneracy break of the E^2_g modes below 9 nm QL thickness, which might be related to an increase of strain. We observed a resonant Raman condition at 1.92 eV laser energy, where two maxima are observed at about 11 and 18 nm QL thickness. The intensity of all main modes considerably enhances due to matching the excitation energy and a van Hove singularity in the density of states. Furthermore, the electron–phonon coupling strength of the A^2_{1g} mode was investigated by the BWF resonance line shape. The Fano parameter ($1/q$) increases from 5 to 24 QLs thickness, indicating that the electron–phonon coupling is robust for the thick layers. This electron–phonon coupling enhancement also contributes to the resonance Raman scattering. These results are a complete picture of the electron and phonon properties and their dependency on the numbers of layers of the Bi_2Te_3 systems.

Author contributions

V. C., B. R. C., and M. T. conceived the idea and wrote the manuscript with inputs from all authors. V. C. carried out the sample synthesis and characterization. S. H. S worked on the data analysis. L. S. and P. M. V. did the first principle calculations. Finally, all the authors discussed the results and commented on and revised the manuscript.

Conflicts of interest

The authors declare no competing financial interest.

Acknowledgements

V. C. acknowledges the CNPq and FAPERJ grants numbers 429773/2018-8, 304144/2018-5 end E-26/010.000980/2019. B. R. C., L. S., P. V. acknowledges the financial support from the Brazilian agencies CAPES and CNPq. M. T. acknowledges the Air Force Office of Scientific Research grant number 158198. We acknowledge Simin Feng for the aid in the AFM measurements.

Notes and references

1 C. Chen, Z. Xie, Y. Feng, H. Yi, A. Liang, S. He, D. Mou, J. He, Y. Peng, X. Liu, Y. Liu, L. Zhao, G. Liu, X. Dong, J. Zhang, L. Yu, X. Wang, Q. Peng, Z. Wang, S. Zhang, F. Yang, C. Chen, Z. Xu and X. J. Zhou, *Sci. Rep.*, 2013, **3**, 2411.
2 H. Zhang, C.-X. Liu, X.-L. Qi, X. Dai, Z. Fang and S.-C. Zhang, *Nat. Phys.*, 2009, **5**, 438–442.
3 M. Z. Hasan and C. L. Kane, *Rev. Mod. Phys.*, 2010, **82**, 3045–3067.
4 M. S. Bahramy, P. D. C. King, a. de la Torre, J. Chang, M. Shi, L. Patthey, G. Balakrishnan, P. Hofmann, R. Arita, N. Nagaosa and F. Baumberger, *Nat. Commun.*, 2012, **3**, 1157–1159.
5 L. Fu and C. L. Kane, *Phys. Rev. Lett.*, 2008, **100**, 096407.
6 Y. Xu, I. Miotkowski, C. Liu, J. Tian, H. Nam, N. Alidoust, J. Hu, C.-K. Shih, M. Z. Hasan and Y. P. Chen, *Nat. Phys.*, 2014, **10**, 956–963.

7 Y. L. Chen, J. G. Analytis, J.-H. Chu, Z. K. Liu, S.-K. Mo, X. L. Qi, H. J. Zhang, D. H. Lu, X. Dai, Z. Fang, S. C. Zhang, I. R. Fisher, Z. Hussain and Z.-X. Shen, *Science*, 2009, **325**, 178–181.
8 D. Teweldebrhan, V. Goyal and A. a. Balandin, *Nano Lett.*, 2010, **10**, 1209–1218.
9 G. Wang, X. G. Zhu, Y. Y. Sun, Y. Y. Li, T. Zhang, J. Wen, X. Chen, K. He, L. L. Wang, X. C. Ma, J. F. Jia, S. B. Zhang and Q. K. Xue, *Adv. Mater.*, 2011, **23**, 2929–2932.
10 Y.-Y. Li, G. Wang, X.-G. Zhu, M.-H. Liu, C. Ye, X. Chen, Y.-Y. Wang, K. He, L.-L. Wang, X.-C. Ma, H.-J. Zhang, X. Dai, Z. Fang, X.-C. Xie, Y. Liu, X.-L. Qi, J.-F. Jia, S.-C. Zhang and Q.-K. Xue, *Adv. Mater.*, 2010, **22**, 4002–4007.
11 G. Zhang, H. Qin, J. Teng, J. Guo, Q. Guo, X. Dai, Z. Fang and K. Wu, *Appl. Phys. Lett.*, 2009, **95**, 53114.
12 C. X. Liu, H. Zhang, B. Yan, X. L. Qi, T. Frauenheim, X. Dai, Z. Fang and S. C. Zhang, *Phys. Rev. B*, 2010, **81**, 2–5.
13 K. Hoefer, C. Becker, D. Rata, J. Swanson, P. Thalmeier and L. H. Tjeng, *Proc. Natl. Acad. Sci. U. S. A.*, 2014, **111**, 14979–14984.
14 C. Li, T. Winzer, A. Walsh, B. Yan, C. Stampfl and A. Soon, *Phys. Rev. B*, 2014, **90**, 1–7.
15 L. Seixas, L. B. Abdalla, T. M. Schmidt, A. Fazzio and R. H. Miwa, *J. Appl. Phys.*, 2013, **113**, 2011–2015.
16 I. Garate, *Phys. Rev. Lett.*, 2013, **110**, 046402.
17 K. Saha and I. Garate, *Phys. Rev. B: Condens. Matter Mater. Phys.*, 2014, **89**, 205103.
18 A. Jorio, R. Saito, G. Dresselhaus and M. S. Dresselhaus, *Raman Spectroscopy in Graphene Related Systems*, Wiley-VCH, Berlin, 2011.
19 V. Carozo, C. M. Almeida, B. Fragneaud, P. M. Bedê, M. V. O. Moutinho, J. Ribeiro-Soares, N. F. Andrade, A. G. Souza Filho, M. J. S. Matos, B. Wang, M. Terrones, R. B. Capaz, A. Jorio, C. A. Achete and L. G. Cançado, *Phys. Rev. B: Condens. Matter Mater. Phys.*, 2013, **88**, 085401.
20 J. Zhang, Z. Peng, A. Soni, Y. Zhao, Y. Xiong, B. Peng, J. Wang, M. S. Dresselhaus and Q. Xiong, *Nano Lett.*, 2011, **11**, 2407–2414.
21 X.-L. Qi and S.-C. Zhang, *Rev. Mod. Phys.*, 2011, **83**, 1057–1110.
22 Y. Xia, D. Qian, D. Hsieh, L. Wray, A. Pal, H. Lin, A. Bansil, D. Grauer, Y. S. Hor, R. J. Cava and M. Z. Hasan, *Nat. Phys.*, 2009, **5**, 18.
23 K. He, Y. Zhang, K. He, C.-Z. Chang, C.-L. Song, L.-L. Wang, X. Chen, J.-F. Jia, Z. Fang, X. Dai, W.-Y. Shan, S.-Q. Shen, Q. Niu, X.-L. Qi, S.-C. Zhang, X.-C. Ma and Q.-K. Xue, *Nat. Phys.*, 2010, **6**, 584–588.
24 G. Hao, X. Qi, Y. Liu, Z. Huang, H. Li, K. Huang, J. Li, L. Yang and J. Zhong, *J. Appl. Phys.*, 2012, **111**, 1–6.
25 D. Kong, W. Dang, J. J. Cha, H. Li, S. Meister, H. Peng, Z. Liu and Y. Cui, *Nano Lett.*, 2010, **10**, 2245–2250.
26 U. Fano, *Phys. Rev.*, 1961, **124**, 1866–1878.
27 S. D. Brown, A. Jorio, P. Corio, M. S. Dresselhaus, G. Dresselhaus, R. Saito and K. Kneipp, *Phys. Rev. B: Condens. Matter Mater. Phys.*, 2001, **63**, 1–8.
28 R. He, Z. Wang, R. L. J. Qiu, C. Delaney, B. Beck, T. E. Kidd, C. C. Chancey and X. P. a. Gao, *Nanotechnology*, 2012, **23**, 455703.
29 Y. Zhao, X. Luo, J. Zhang, J. Wu, X. Bai, M. Wang, J. Jia, H. Peng, Z. Liu, S. Y. Quek and Q. Xiong, *Phys. Rev. B: Condens. Matter Mater. Phys.*, 2014, **90**, 245428.
30 S. Xu, Y. Han, X. Chen, Z. Wu, L. Wang, T. Han, W. Ye, H. Lu, G. Long, Y. Wu, J. Lin, Y. Cai, K. M. Ho, Y. He and N. Wang, *Nano Lett.*, 2015, **15**, 2645.
31 Y. Jiang, X. Zhang, Y. Wang, N. Wang, D. West, S. Zhang and Z. Zhang, *Nano Lett.*, 2015, **15**, 3147–3152.
32 P. Giannozzi, O. Andreussi, T. Brumme, O. Bunau, M. B. Nardelli, M. Calandra, R. Car, C. Cavazzoni, D. Ceresoli, M. Cococcioni, N. Colonna, I. Carnimeo, A. D. Corso, S. de Gironcoli, P. Delugas, R. A. DiStasio, A. Ferretti, A. Floris, G. Fratesi, G. Fugallo, R. Gebauer, U. Gerstmann, F. Giustino, T. Gorni, J. Jia, M. Kawamura, H.-Y. Ko, A. Kokalj, E. Küçükbenli, M. Lazzeri, M. Marsili, N. Marzari, F. Mauri, N. L. Nguyen, H.-V. Nguyen, A. Otero-de-la Roza, L. Paulatto, S. Poncé, D. Rocca, R. Sabatini, B. Santra, M. Schlipf, A. P. Seitsonen, A. Smogunov, I. Timrov, T. Thonhauser, P. Umari, N. Vast, X. Wu and S. Baroni, *J. Phys.: Condens. Matter*, 2017, **29**, 465901.
33 P. E. Blöchl, *Phys. Rev. B: Condens. Matter Mater. Phys.*, 1994, **50**, 17953–17979.
34 J. P. Perdew and A. Zunger, *Phys. Rev. B: Condens. Matter Mater. Phys.*, 1981, **23**, 5048–5079.
35 J. P. Perdew, K. Burke and M. Ernzerhof, *Phys. Rev. Lett.*, 1996, **77**, 3865–3868.
36 L. Fu and C. L. Kane, *Phys. Rev. B: Condens. Matter Mater. Phys.*, 2007, **76**, 045302.
37 Y.-x. Yuan, L. Ling, X.-y. Wang, M. Wang, R.-a. Gu and J.-l. Yao, *J. Raman Spectrosc.*, 2007, **38**, 1280–1287.
38 W. Richter, H. Köhler and C. R. Becker, *Phys. Status Solidi B*, 1977, **84**, 619–628.
39 J. O. Jenkins, J. A. Rayne and R. W. Ure, *Phys. Rev. B: Condens. Matter Mater. Phys.*, 1972, **6**, 1609.
40 B. Y. Yavorsky, N. F. Hinsche, I. Mertig and P. Zahn, *Phys. Rev. B: Condens. Matter Mater. Phys.*, 2011, **84**, 165208.
41 C. Lee, H. Yan, L. E. Brus, T. F. Heinz, J. Hone and S. Ryu, *ACS Nano*, 2010, **4**, 2695–2700.
42 S. Baroni, S. de Gironcoli, A. Dal Corso and P. Giannozzi, *Rev. Mod. Phys.*, 2001, **73**, 515–562.
43 R. Saito, M. Hofmann, G. Dresselhaus, A. Jorio and M. S. Dresselhaus, *Adv. Phys.*, 2011, **60**, 413–550.
44 R. Gupta, Q. Xiong, C. K. Adu, U. J. Kim and P. C. Eklund, *Nano Lett.*, 2003, **3**, 627–631.
45 C. Attaccalite, L. Wirtz, M. Lazzeri, F. Mauri and A. Rubio, *Nano Lett.*, 2010, **10**, 1172–1176.